

# Density–Nematic Coupling in Isotropic Linear Polymers: Acoustic and Osmotic Birefringence

Aleksandar Popadić, Daniel Svenšek,\* Rudolf Podgornik, and Matej Praprotnik

Linear polymers and other connected “line liquids” exhibit a geometrical coupling between density and equilibrium orientational order on the macroscopic level that gives rise to a Meyer-de Gennes vectorial conservation law for polar orientational order, or its amended version for apolar nematic order when described as “recovered” polar order. They generally exhibit fluctuations of orientational order, starting with its lowest moment, the polar order, which in the isotropic phase is geometrically decoupled from density. As a contrast, quadrupolar (nematic) orientational fluctuations are inherently coupled to density fluctuations already in the isotropic system and not subject to the existence of an orientational phase transition. To capture this, it takes the tensorial description of the nematic order, leading to a geometrical coupling between density and orientational order in the form of a tensorial conservation law. This coupling implies that a spatial density variation will induce nematic order and thereby an acoustic or osmotic optical birefringence even in isotropic phase. The theory is validated by performing detailed Monte Carlo simulations of isotropic melts and comparing the results with macroscopic predictions. This also exposit a means of determining the macroscopic parameters by microscopic simulations to yield realistic continuum models of specific polymeric materials.

## 1. Introduction

Isotropic liquids possess no macroscopic preferred direction. Nevertheless, if they consist of non-spherical microscopic elementary units like prolate, oblate, or more complicated shapes, they do exhibit collective fluctuations of orientational order of these microscopic units. The fluctuating orientational order is systematically described by fluctuating moments of the orientational distribution function, starting with its dipole moment characterizing polar orientational order, quadrupole moment describing the more common nematic orientational order, octupole moment describing tetrahedric order<sup>[1]</sup> and so on.

Governed by symmetry, orientational order is generally coupled to other system variables or external fields. However, in an isotropic system such effects are macroscopically significant only when the system is in the vicinity of an orientational phase transition (if it exists) like the transition from the isotropic to the nematic phase,

where orientational fluctuations become large and orientational order gets more susceptible to the influence of external and other internal variables.

In systems featuring a reduction of microscopic degrees of freedom (e.g., the connectivity of a polymer chain presents a microscopic constraint reducing the configurational space of the monomers in comparison with non-polymerized monomers), however, the coupling of the orientational order to the displacement field, in particular to density variations, is a geometric necessity and is not related to the proximity of an orientational phase transition threshold or its very existence. Moreover, being geometrical (unbreakable) rather than energetic, such constraint is inherently robust and is hardly affected by any system variables except those that enter the constraint explicitly. As such, the response dictated by this constraint is well-defined, universal, and remains unaltered when the system traverses its path in the parameter space.

It has been recognized several decades ago that a microscopic geometric constraint of a continuous contour line in the case of the so-called *line liquids*<sup>[2–4]</sup> — including magnetic flux lines as a vortex liquid in type II superconductors, chains of particles in ferro- and electrorheological fluids formed in an external field, and chains of connected monomers in main-chain polymer nematics — implies a constraint on macroscopic continuum fields used to describe the coarse-grained configuration of


Dr. A. Popadić, Prof. M. Praprotnik  
Laboratory for Molecular Modeling  
National Institute of Chemistry  
SI-1001 Ljubljana, Slovenia

Prof. D. Svenšek, Prof. R. Podgornik  
Department of Physics, Faculty of Mathematics and Physics  
University of Ljubljana  
SI-1000 Ljubljana, Slovenia  
E-mail: daniel.svensek@fmf.uni-lj.si

Prof. R. Podgornik  
Department of Theoretical Physics  
J. Stefan Institute  
SI-1000 Ljubljana, Slovenia

Prof. R. Podgornik  
School of Physical Sciences and Kavli Institute for Theoretical Sciences  
University of Chinese Academy of Sciences  
Beijing 100049, China

Prof. R. Podgornik  
CAS Key Laboratory of Soft Matter Physics, Institute of Physics  
Chinese Academy of Sciences  
Beijing 100190, China

 The ORCID identification number(s) for the author(s) of this article can be found under <https://doi.org/10.1002/adts.201900019>

DOI: 10.1002/adts.201900019

such continuous contour lines. That is, even if we do not have access to probing the microscopic structure directly, we can nevertheless detect the presence of the microscopic continuity constraint through a macroscopic response of the system.

In linear (main-chain) nematic polymers, the continuity constraint was derived in the form of the so-called vectorial conservation law for the “polymer current” density<sup>[5]</sup> that incorporates the full orientational order vector  $\mathbf{a}(\mathbf{r})$ ,  $|\mathbf{a}| \leq 1$ , as:  $\nabla \cdot (\rho l_0 \mathbf{a}) = \rho^\pm$ , where  $\rho(\mathbf{r})$  is the volume density of arbitrary segments (e.g., monomers) of length  $l_0$ . This generalizes the previously proposed<sup>[2,6–13]</sup> Meyer–de Gennes continuity constraint  $\nabla \cdot (\rho_s \mathbf{n}) = \rho^\pm$ , coupling splay deformation of the nematic director  $\mathbf{n}(\mathbf{r})$  with variations of areal density of chains  $\rho_s(\mathbf{r})$  (i.e., “geometrical” flux density of the chains,  $\rho_s = \rho l_0 |\mathbf{a}|$ ). The consequence of the continuity constraint is that the density of long chains decreases as they are splayed, since there are too few chain ends available that would be able to populate the ensuing voids between the chains. Shorter chains, on the other hand, provide more ends which can fill the voids more easily. This distinction is captured by the volume density  $\rho^\pm(\mathbf{r}) = \rho^+(\mathbf{r}) - \rho^-(\mathbf{r})$  of chain beginnings (+) and endings (−), which then acts as a source in the continuity equation. Moreover, it is clear by construction<sup>[14]</sup> that in this conservation law,  $\mathbf{a}(\mathbf{r}) = \langle \mathbf{t} \rangle$  is exactly the coarse-grained (mesoscopic) polar orientational order of polymer chain tangents  $\mathbf{t}$ . In its elementary form, this conservation law thus rigorously applies to (possible) polar orientational order of the polymer rather than its nematic order.

In liquids, equilibrium polar order is rare. If they consist of polar building blocks as they readily do, polar orientational fluctuations are, however, inherent. In a homogeneous isotropic system, we have  $\rho = \rho_0$ ,  $\mathbf{a} = 0$ , and  $\rho^\pm = 0$  in equilibrium. Any deviation  $\delta\rho(\mathbf{r})$ ,  $\delta\mathbf{a}(\mathbf{r})$  must satisfy the vectorial conservation law constraint to the lowest order as:  $\rho_0 l_0 \nabla \cdot \delta\mathbf{a} = \delta\rho^\pm$ , that does not involve the density variation, which is thus unaffected by this constraint. In other words, the polymer chain connectivity does not induce any coupling of the density fluctuations and the polar orientational order fluctuations in an isotropic polymeric liquid.

Nematic (quadrupolar) orientational order is, however, described by the traceless nematic order tensor  $Q_{ij}(\mathbf{r}) = \frac{3}{2} \langle (t_i t_j) - \frac{1}{3} \delta_{ij} \rangle$ , where for linear polymers the averaging is again over chain tangents in a mesoscopic volume centered at  $\mathbf{r}$ . A rigorous conservation law can be derived not only for the polar order, but also for the quadrupolar order of the chains, which, unlike the polar order, is insensitive to the chain backfolding.<sup>[5,15]</sup> A completely general form of this tensorial conservation law (see Section S1, Supporting Information, for formal derivation) for arbitrary number of chains with arbitrary length and flexibility is then

$$\partial_j \left[ \rho \left( Q_{ij} + \frac{1}{2} \delta_{ij} \right) \right] = \frac{3}{2} \frac{1}{l_0} g_i + \frac{3}{2} \rho k_i \quad (1)$$

where the volume density  $\mathbf{g}(\mathbf{r})$  of chain end tangents, defined as pointing inward, and the average chain curvature vector  $\mathbf{k}(\mathbf{r})$ , multiplied by the density, both play the role of the sources in this continuity equation and can be furthermore considered as independent for sufficiently long chains. The average chain curvature vector source reflects the effect of the chain folds, which can fill the voids created by splay in a similar way as chain ends do. The stiffer and longer the chains, the more expensive are the sources

and the stronger is the constraint. Similarly to the vectorial case, the tensorial analogue in Equation (1) is an exact macroscopic implication of the microscopic polymer chain connectivity.

We have theoretically and numerically shown<sup>[14]</sup> that it is possible to amend the vectorial continuity equation by introducing the “recovered” polar order,<sup>[14,15]</sup> such that it can be rigorously applied to the *uniaxial* nematic phase with general chain backfolding. Nevertheless, a complete description of the nematic phase should be based on the full nematic Q-tensor and the corresponding continuity constraint (Equation (1)), which is needed if biaxiality is important or topological (half-integer) defects of the nematic phase are considered. In the isotropic phase, however, nematic fluctuations are inherently tensorial and *cannot* be described otherwise than with the Q-tensor. Consequently, for a consistent description the tensorial continuity equation must be inevitably used in this case — a situation, which has not been considered hitherto.

In equilibrium,  $Q_{ij} = 0$  and a deviation  $\delta Q_{ij}$  must satisfy the constraint in Equation (1), that to the lowest order yields

$$\rho_0 \partial_j \delta Q_{ij} + \frac{1}{2} \partial_i \delta \rho = \frac{3}{2} \frac{1}{l_0} \delta g_i + \frac{3}{2} \rho_0 \delta k_i \quad (2)$$

Therefore, unlike the fluctuations of polar ordering, the fluctuations of nematic (quadrupolar) ordering and density are generally coupled to the first order even in an orientationally disordered, isotropic phase (Figure 1). This situation is quite generic and applies in principle to any linear polymer melt/solution, for example, DNA and other biopolymers, as well as synthetic polymers like polyethylene, polyvinyls, polyamides, polyesters, polystyrene, polycarbonates etc. The nematic order–density coupling is particularly strong in the case of long and stiff polymer chains, since there the fluctuations of the r.h.s. of Equation (2) are costlier and thus weaker. But as we will show, it can be significant already for chains as short as a couple of units.

Thus, the tensorial constraint has profound implications already for the isotropic phase. A quick inspection of Equation (2) shows that a fluctuation with the wave vector in  $z$  direction (keeping in mind that in the isotropic system all directions are equivalent) couples  $\delta\rho$  and  $\delta Q_{zz}$ . Hence, a spatial variation of density or concentration will induce nematic order and thereby optical anisotropy in an otherwise isotropic system. We will show that this constraint gives rise to a class of interesting and unanticipated macroscopic phenomena in linear polymers, like acoustic birefringence in polymer melts or osmotic birefringence in polymer solutions.

Moreover, we also present a methodology that enables one to determine the parameters of the continuum description of the isotropic polymeric liquid employing microscopic simulations. This bears some resemblance to well-established derivations of coarse-grained potentials in molecular simulations, for example, coarse-graining with the relative entropy.<sup>[16–18]</sup> By using known atomistic or coarse-grained force fields of specific linear polymers, it is possible to accurately extract from numerically calculated correlation functions realistic values of the macroscopic parameters that correspond to the specific polymeric material. In this light, microscopic simulations of dense phases of DNA<sup>[19,20]</sup> can fix the parameters of coarse-grained, continuum descriptions used, for example, to study the packing and ordering properties

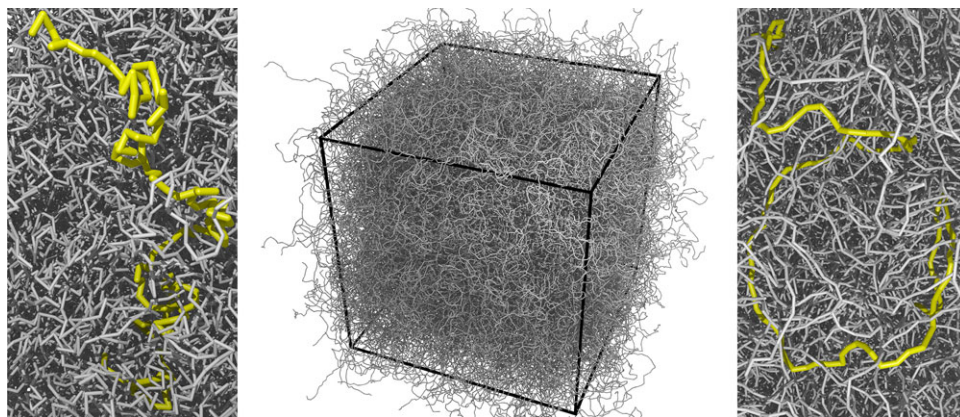


**Figure 1.** Middle: snapshot of the simulated isotropic polymer melt with  $2^{18}$  monomers (2048 chains with  $N_s = 128$  segments) employing periodic boundary conditions. Assuming for the monomer diameter the distance at which the repulsive potential is equal to  $k_B T$ , we estimate the polymer volume fraction to  $\approx 0.11$ , corresponding to a polymer melt. The close-ups highlight a single chain in the ideally flexible ( $\epsilon = 0$ , left) and semiflexible ( $\epsilon = 4.926 k_B T$ , right) case.

of nano-confined DNA as in, for example, viral capsids<sup>[21,22]</sup> or nanochannels.<sup>[23,24]</sup>

## 2. Correlation Functions of Collective Fluctuations: Comparison with Microscopic Simulations

The complete set of Fourier-component correlators describing the thermodynamic spatial correlations is derived as (see Section S2, Supporting Information, for derivation)

$$\langle |\delta Q_{xy}|^2 \rangle = \frac{k_B T}{2} \frac{N_0}{\rho_0} \frac{1}{A + Lq^2} \quad (3)$$

$$\langle |\delta Q_{\{xz, yz\}}|^2 \rangle = \frac{k_B T}{2} \frac{N_0}{\rho_0} \frac{1}{A + (L + \frac{1}{2}\tilde{G})q^2} \quad (4)$$

$$\langle |\delta Q_{zz}|^2 \rangle = \frac{k_B T}{2} \frac{4N_0}{\rho_0} \left[ 3A + \left( 3L + \frac{8\tilde{G}\tilde{B}}{4\tilde{B} + \tilde{G}q^2} \right) q^2 \right]^{-1} \quad (5)$$

$$\langle |\delta \tilde{\rho}|^2 \rangle = \frac{k_B T}{2} \frac{8N_0}{\rho_0} \left[ 4\tilde{B} + \frac{3\tilde{G}(A + Lq^2)q^2}{3A + (3L + 2\tilde{G})q^2} \right]^{-1} \quad (6)$$

$$\begin{aligned} & \langle \delta \tilde{\rho}^* \delta Q_{zz} + \delta \tilde{\rho} \delta Q_{zz}^* \rangle / 2 \\ &= - \frac{k_B T}{2} \frac{N_0}{\rho_0} \frac{8\tilde{G}q^2}{12A\tilde{B} + [12\tilde{B}L + (3A + 8\tilde{B})\tilde{G}]q^2 + 3\tilde{G}Lq^4} \quad (7) \end{aligned}$$

where  $B$  is the bulk modulus,  $\rho_0$  is the volume number density of monomers,  $A$  is the “nematic order stiffness,”  $B'$  and  $L$  (the nematic elastic constant) are penalizing  $\rho$  and  $Q$  gradients and  $\tilde{B} = B + B'q^2$ . The constraint due to the tensorial conservation law is taken into account by a quadratic potential penalizing its sources, where  $G(\frac{2}{3}\rho_0 l_0)^2 \equiv \tilde{G}$  is the strength of the constraint connected with the free-energy cost of the sources (see Section S2, Supporting Information, for details). Importantly, since the system is isotropic there is no elastic anisotropy and thus the difference between the fluctuations  $\delta Q_{xy}$  and  $\delta Q_{\{xz, yz\}}$  is

a signature of the tensorial constraint alone. From the correlators in Equations (3) and (4) one can efficiently determine the values of the parameters  $A$ ,  $L$ , and the coupling strength  $\tilde{G}$ , which we will make use of in the following.

The coupling of the fluctuations  $\delta Q_{zz}$  and  $\delta \tilde{\rho}$  is reflected in a nonzero cross-correlation, Equation (7). This negative correlation is again the signature of the tensorial constraint and vanishes in the absence of the constraint when  $\delta \tilde{\rho}$  and  $\delta Q_{zz}$  are decoupled.

To confirm the existence of the tensorial constraint, we employ Monte Carlo (MC) simulations of discrete worm-like chains (WLC), and compare the simulated correlation functions of static long wavelength fluctuations with Equations (3) to (7) following from the continuum theory. Validating the predictions of the macroscopic theory with molecular-level computer simulations of polymers<sup>[25–28]</sup> is challenging, since such simulations must i) address the long-wavelength limit and ii) realize different regimes of chain backfolding (hairpin formation). Thus, it is essential to consider large systems of preferably long polymer chains,<sup>[29]</sup> where the sampling must include statistically independent (decorrelated) configurations. We fulfill these requirements benefiting from a recently developed mesoscopic model<sup>[14,30]</sup> of discrete WLCs. The modeled system contains  $N_c$  WLCs comprised of  $N_s$  linearly connected segments of fixed length  $l_0$ . Consecutive segments are subjected to a standard angular potential (see Section S3, Supporting Information) with strength  $\epsilon$  controlling the WLC bending stiffness. Moreover, all segments possess a non-bonded isotropic repulsive interaction with finite microscopic range  $2l_0$  and strength  $\kappa$ . See Section S3, Supporting Information and ref.<sup>[14]</sup> for details of the numerical method and the simulated mesoscopic WLC model.

We study large isotropic melt systems containing  $N_0 = N_c N_s = 2^{18}$  segments. An example of the simulation snapshot is shown in Figure 1 (middle). The configurations are equilibrated through MC starting from a nematic phase, with the chains stretched along the  $z$  axis of the laboratory frame and their centers of mass randomly distributed in a cubic box with periodic boundary conditions. The MC algorithm utilizes the standard<sup>[31,32]</sup> slithering-snake moves, as well as volume fluctuation moves at pressure  $Pl_0^3/(k_B T) = 2.87$  resulting in simulation

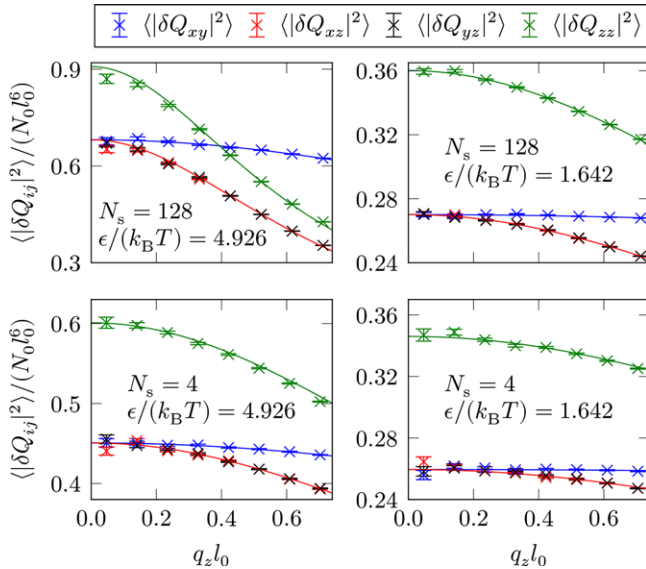


**Figure 2.** Nematic  $(\delta Q_{ij})$  fluctuations of stiffer ( $\epsilon = 4.926 k_B T$ , left) and more flexible ( $\epsilon = 1.642 k_B T$ , right) chains with  $N_s = 128$  (top) and  $N_s = 4$  (bottom) segments, fitted with Equations (3) and (4) to extract the values of the parameters  $A$ ,  $L$  and  $\tilde{C}$ . The  $\langle |\delta Q_{zz}|^2 \rangle$  curves are not fitted but are direct plots of the theoretical result in Equation (5).

box sides of length  $\langle L \rangle / l_0 \sim 66$  and system's volume fluctuations of  $\sim 0.1\%$ . While working in the isothermal-isobaric ensemble is computationally more expensive, it is useful when determining the bulk modulus. The efficient soft model enables us to accumulate large sequences of statistically decorrelated isotropic configurations, which allow for direct validation of the macroscopic theory via the correlations in Equations (3) to (7) (see Section S3, Supporting Information, for details of their extraction from simulation data).

**Figure 2** shows examples of normalized fluctuations  $\langle |\delta Q_{ij}|^2 \rangle$  of the nematic ordering, calculated in simulations, for different chain lengths (top, bottom) and different chain flexibilities (left, right). While  $\langle |\delta Q_{xz}|^2 \rangle$  and  $\langle |\delta Q_{yz}|^2 \rangle$  coincide, it is confirmed that they are different from the fluctuations  $\langle |\delta Q_{xy}|^2 \rangle$ , in accord with the results in Equations (3) and (4). The difference grows with the strength  $\tilde{C}$  of the tensorial constraint, increasing with length ( $N_s$ ) and bending stiffness ( $\epsilon$ ) of the chains. The  $\langle |\delta Q_{xy}|^2 \rangle$  points are fitted with Equation (3), determining the parameters  $A$  and  $L$ . With these parameters fixed, the  $\langle |\delta Q_{xz}|^2 \rangle$  and  $\langle |\delta Q_{yz}|^2 \rangle$  data are then fitted with Equation (4) and the strength  $\tilde{C}$  is determined.

It would be natural to determine the modulus  $B$  from the density autocorrelation (the structure factor) in Equation (6). It turns out, however, that the theoretical Lorentzian profile of the structure factor in the continuum picture (Equation (6)) is completely overridden by the influence of the discrete structure of the simulated WLCs even for the lowest  $q$ 's that we can achieve with our simulation box size. Therefore, we put  $B'$  to zero and determine  $B$  from fluctuations  $\delta V$  of the simulation box volume  $V_0$ ,  $\langle \delta V^2 \rangle = V_0 k_B T / B$ . This agrees with the structure factor in Equation (6) for  $q = 0$ , recalling that for a homogeneous density variation,  $\delta V / V_0 = -\delta \rho / \rho_0$  and the Fourier component is  $\delta \rho(q = 0) = V_0 \delta \rho$ .

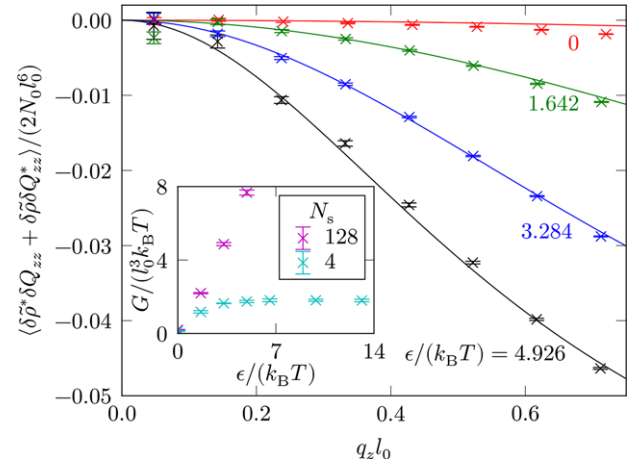


**Figure 3.** Dimensionless density–nematic cross-correlations for chains with length  $N_s = 128$  and varying flexibility. The curves are plots of Equation (7) (no fitting). Inset: the dimensionless coupling strength  $G$  vs. bending stiffness  $\epsilon / (k_B T)$ , determined from fits of the numerically calculated fluctuations  $\langle |\delta Q_{xy}|^2 \rangle$ ,  $\langle |\delta Q_{xz}|^2 \rangle$ ,  $\langle |\delta Q_{yz}|^2 \rangle$  (Figure 2).

A direct display of the density–nematic coupling is the cross-correlation in Equation (7) between  $\delta \tilde{\rho}$  and  $\delta Q_{zz}$ , in theory directly proportional to the strength of the coupling  $\tilde{C}$ . In **Figure 3**, the cross-correlation is shown for several chain flexibilities. Here, the theoretical curves are not fitted, but correspond to the prediction in Equation (7), using the values of the parameters  $A$ ,  $L$ ,  $\tilde{C}$ , and  $B$  extracted from the fluctuations  $\delta Q_{xy}$ ,  $\delta Q_{xz}$ ,  $\delta Q_{yz}$  (Figure 2) and  $\delta V$ . The same is valid for the  $\langle |\delta Q_{zz}|^2 \rangle$  curves in Figure 2, which are plots of Equation (5) with the same parameter values. For sufficiently long chains, the coupling strength  $G$  extracted from the simulation data (Figure 3, inset) clearly increases with chain stiffness, as anticipated from the fact that the fluctuations  $\delta \mathbf{k}$  of the curvature source in Equation 2 get costlier. In the case of very short chains,  $G$  becomes saturated already at lower stiffness, since in this case the source  $\delta \mathbf{g}$ , corresponding to the density of chain end tangents, is dominant (next Section reveals that this is only a partial reason).

**Figure 3** thus presents direct evidence of the connection between density variations and the emergence of nematic orientational order in otherwise isotropic polymeric liquid, which is also well described by the theoretical cross-correlation in Equation (7). Moreover, the strength of this coupling increases for long and stiff chains, as expected and empirically confirmed in the inset of **Figure 3**.

### 3. Strength of the Tensorial Constraint

The coupling strength  $G$  corresponding to the tensorial constraint is derived within a minimalistic model of combined sources (see Section S4, Supporting Information, for details) as

$$G = \frac{3k_B T}{\rho_0^\pm + 2k_B T \rho_0 / \epsilon} \quad (8)$$

where  $\rho_0^\pm$  is the average (equilibrium) volume density of chain ends (in the tensorial formulation, there is no distinction

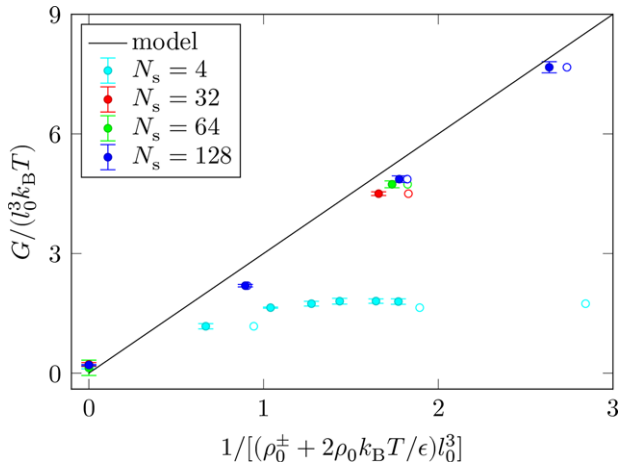


**Figure 4.** Dimensionless strength of the tensorial constraint  $G$ , determined in the simulations for several chain lengths  $N_s$  and bending stiffnesses  $\epsilon$ , versus its dimensionless theoretical expression in Equation (8) (solid circles with statistical error bars) — a direct result without fitted parameters. The contribution of chain ends can be traced with the help of the empty circles, the abscissae of which have  $\rho_0^\pm$  put to zero (three rightmost  $N_s = 4$  open circles fall outside the plot and are not shown).

between chain beginnings and endings — they are unified into a single type of ends, see Section S1, Supporting Information), and consistently crosses over from the chain-end- to the chain-curvature-dominated strength of the constraint. Assuming monodisperse chains with  $N_s$  monomers, such that  $\rho_0^\pm = 2\rho_0/N_s$ , we can rewrite Equation (8) as

$$G = \frac{3}{2} \frac{k_B T}{\rho_0} \frac{1}{1/N_s + l_0/\xi_p} \quad (9)$$

The crossover takes place at  $\xi_p = N_s l_0$ , that is, when the persistence length equals the length of the chain.

Hence, for sufficiently long chains,  $G$  will be dominated by the curvature source for any finite value of the bending stiffness  $\epsilon$ , while the contribution of the end tangents will be less significant. In this case  $G \approx (3/2)\epsilon/\rho_0 = (3/2)k_B T \xi_p / (\rho_0 l_0)$  becomes directly proportional to the bending stiffness, corresponding to the semiflexible regime of severely bent chains. Throughout this regime, which is the dominating one for long chains,  $G$  is set by the chain curvature.

**Figure 4** shows a plot of the dimensionless strength  $G$  of the tensorial constraint, determined in the simulations, versus the dimensionless expression in Equation (8). According to this model, the points should thus lie on the indicated straight line. For all but shortest chains the agreement is remarkable, all the more so since the theoretical prediction in Equation (8) is direct and involves no fitted parameters. The problem with very short chains, in particular if they are stiff, is the strong correlation between end tangents of the chain and the in-between profile of its curvature vector, in other words, a rather small number of internal configurational degrees of freedom of the chain, which is beyond the regime of validity of the model leading to Equation (8).

For the longest chains ( $N_s = 128$ ), the two contributions in the denominator of Equation (8) are, in dimensionless form,  $\rho_0^\pm l_0^3 \sim 0.014$  and  $2\rho_0 l_0^3 k_B T / \epsilon \sim 0.37$  (for  $\epsilon = 4.926 k_B T$ , and

larger for smaller  $\epsilon$ ). For the shortest chains ( $N_s = 4$ ), the figures are  $\rho_0^\pm l_0^3 \sim 0.44$  and  $2\rho_0 l_0^3 k_B T / \epsilon \sim 0.13$  (for  $\epsilon = 13.136 k_B T$ , and larger for smaller  $\epsilon$ ). That is, in the examples shown in Figure 4 the coupling strength  $G$  is indeed determined predominantly by chain curvature, except for the stiffer cases of the shortest chains. Regarding the above discussion, this is in accord with Figure 1 (right), where one can see that the persistence length, while clearly exceeding the monomer length, is still much shorter than the chain.

Moreover, Figure 4 also reveals the relevance of the effective source model: the abscissae of the additional points (empty circles) are obtained by omitting  $\rho_0^\pm$  in Equation (8). Without the contribution of end tangents the agreement is clearly worse — the differing slope of the  $N_s = \{32, 64, 128\}$  case is particularly noteworthy. The improvement when including  $\rho_0^\pm$  is naturally largest for the shortest chains, where the theory, however, breaks down for the reason mentioned above.

As exhibited in Figure 4, for all considered cases the coupling is somewhat weaker than predicted by Equation (8). Plausibly, this slight overall weakening of the constraint is a signature of the fact that the curvature source  $\delta\mathbf{k}$  is not autonomous, as assumed in the model, but is generally coupled to gradients of  $\delta\rho$  and  $\delta Q_{ij}$ . A systematic study to quantify all such symmetry-allowed couplings as additions to the free-energy functional is a natural next step. In this context, it may seem surprising that the theoretical prediction of the average curvature in Figure S1, Section S5, Supporting Information, which assumes independent pairs of segments, is so accurate. In general, one would expect it to be influenced by these couplings as well. It is, however, physically reasonable that they affect the direction of the curvature fluctuations  $\delta\mathbf{k}$  significantly more than their magnitude. In other words, the magnitude  $\langle |\delta\mathbf{k}|^2 \rangle$  is inertly fixed by the free-energy cost whereas the direction of  $\delta\mathbf{k}$  is not distinguished and is therefore prone to other, weaker energy couplings. For increasingly stiff chains, these become inferior compared to the increasing energy cost of the curvature, which in Figure 4 seems to be the reason for the improving agreement in the case of stiffer  $N_s = 128$  chains.

## 4. Discussion

Once the coupling strength  $\tilde{C}$  has been determined, for example, from analysis of the fluctuations as shown, also the equilibrium coupling of  $\delta\rho$  and  $\delta Q$  is known. Through this coupling, density or concentration inhomogeneities induce orientational order of the polymer chains, which furthermore results in a uniaxial dielectric tensor  $\epsilon_{ij} = \epsilon\delta_{ij} + \frac{2}{3}\epsilon_a\delta Q_{ij}$  with an anisotropy  $\epsilon_{zz} - \epsilon_{\perp} = \epsilon_a\delta Q_{zz}$ , where  $\epsilon$  is the dielectric constant of the isotropic phase and  $\epsilon_a$  the dielectric anisotropy of a phase with perfect orientational order of the chains (maximum possible anisotropy of the material).

The anisotropy of the dielectric constant implies birefringent optical response. For example, a density (acoustic) plane wave  $\delta\tilde{\rho}(\mathbf{r}, t) = \delta\rho(\mathbf{r}, t)/\rho_0$  with wave vector  $\mathbf{q} = q\hat{\mathbf{e}}_z$  induces uniaxial nematic ordering along  $z$  (see Section S6, Supporting Information). The ordering is oblate ( $\delta Q_{zz} < 0$ ) in compressions and prolate ( $\delta Q_{zz} > 0$ ) in rarefactions. The induced nematic order gives rise to the dielectric anisotropy

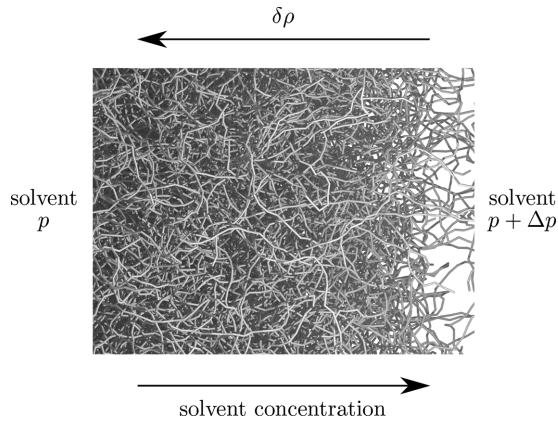


**Figure 5.** Schematic depiction of polymer concentration gradient,  $\nabla\delta\rho$ , sustained by solvent osmotic pressure difference,  $\Delta p$ , between a pair of bounding semipermeable membranes. If the chains are long and rather rigid, they accommodate the concentration gradient primarily by prolate/oblate orientational ordering.

$$(\varepsilon_{zz} - \varepsilon_{\perp})(\mathbf{r}, t) = -\frac{\varepsilon_a}{2} \frac{\bar{G}q^2}{A + (L + \bar{G})q^2} \delta\bar{\rho}(\mathbf{r}, t) \quad (10)$$

For a dynamic disturbance,  $\bar{G}$  is expected to increase substantially above its static value determined from the static fluctuations, as the inverse frequency becomes comparable to and falls below a characteristic dynamic time of the sources of the continuity equation (Equation (1)), where the disentanglement time<sup>[33–37]</sup> of the polymer chains seems to play an important role. Acoustically induced dielectric anisotropy, Equation (10), is nevertheless small, as relative density variations due to acoustic excitations are normally tiny. Note that an acoustic reorienting effect can be substantial in conventional non-polymeric nematic liquid crystals,<sup>[38]</sup> which is attributed to the coupling of density with the symmetry variable (nematic director) rather than to the tensorial (geometric) constraint for rod-like molecules acting as short chains.

In polymers, a much stronger effect can be expected in polymer solutions, where  $\delta\rho$  represents polymer concentration variations rather than variations of the polymer melt density. **Figure 5** presents a schematic situation, where a 1D polymer concentration gradient  $\nabla\delta\rho = \hat{\mathbf{e}}_z\partial_z\delta\rho$  is sustained by a difference in solvent osmotic pressure imposed by a pair of membranes at  $z = \pm d/2$ , permeable only to the solvent. Assuming that  $(\partial_z\delta\rho)/\rho$  is small and constant, and choosing that the system be isotropic in the middle,  $\delta Q_{zz}(z=0) = 0$ , we get an exponential profile of  $\delta Q_{zz}$  (see Section S6, Supporting Information) and hence of the induced dielectric anisotropy

$$(\varepsilon_{zz} - \varepsilon_{\perp})(z) \approx -\frac{\varepsilon_a}{4} \frac{G'\xi\rho}{L + G'\rho^2} \frac{\partial_z\delta\rho}{\cosh(d/(2\xi))} \frac{\sinh(z/\xi)}{\cosh(d/(2\xi))} \quad (11)$$

where  $G' = G(\frac{2}{3}l_0)^2$  and  $\xi \sim \sqrt{L/A}$  is the nematic correlation length. That is, as a response to a constant concentration gradient, the nematic order and dielectric tensors are modulated in the boundary layers with characteristic thickness of the nematic correlation length  $\xi$ . Quite generally it is thus expected that, in the presence of a normal concentration gradient, any boundaries

are typically decorated with short-range uniaxial nematic ordering/dielectric anisotropy in the normal direction.

When the concentration gradient is not constant, however, nematic ordering is induced globally. In lowest order, for the variation of the dielectric anisotropy, induced by  $\partial_z\delta\rho(z)$  that varies slowly on the scale of  $\xi$ , we have (see Section S6, Supporting Information)

$$\partial_z^2(\varepsilon_{zz} - \varepsilon_{\perp}) \approx -\frac{\varepsilon_a}{2} \frac{G'\rho}{L + G'\rho^2} \partial_z^2\delta\rho \quad (12)$$

A meaningful example is that with spherical symmetry: consider a spherical boundary of the solvent-rich side (the right boundary in Figure 5, e.g., a membrane or an interface of a bubble, representing a spherical source of constant flux  $\Phi$  of the solvent into the surrounding bulk (let the other boundary be absent or far away). Based on diffusion, it is reasonable to assume that for an overall constant density the profile of the polymer concentration at a sufficient distance  $r$  from the center of the bubble will be

$$\rho(r) = \rho_0 - \Phi/(4\pi Dr) \quad (13)$$

with  $\rho_0$  its bulk concentration and  $D$  the diffusivity. Consequently, for a system which is isotropic in the bulk we expect that such spherical inhomogeneity will induce uniaxial ordering of the chains in the radial direction (see Section S6, Supporting Information). The corresponding dielectric anisotropy in the limit of sufficiently large  $r$  is then

$$(\varepsilon_{rr} - \varepsilon_{\perp})(r) \approx -\varepsilon_a \frac{G'\rho_0}{6L + G'\rho_0^2} \frac{\Phi}{4\pi Dr} \quad (14)$$

Interestingly, in the considered regime the induced nematic ordering is negative, that is, oblate, rather than prolate as one might have naively guessed from the decreasing polymer concentration. Note that in all of the in Equations (10) to (14) the polymer density appears in the form of the product  $\rho_{(0)}l_0$ , that is, the total length of the polymer per unit volume, which is the relevant volume density for the coupling.

Such optical effects due to the dielectric anisotropy, resulting from concentration variations in solutions of long linear polymers with limited flexibility, should be observable, for example, as an *osmotic birefringence*. The phenomenon is akin to shear flow-induced birefringence in fluid polymers and stress-optic law in elastic solid dielectric materials, that is, the direct coupling between the strain and the dielectric tensors. The key distinction is, however, that the osmotic-stress-induced birefringence takes place in a static liquid, where there exists no strain/strain rate tensor that could couple to the dielectric tensor. In this case, the coupling — which is a manifestation of the microscopic geometrical constraint — is via the concentration gradient through the tensorial continuity equation, Equation (1).

It is challenging to determine the macroscopic parameters of real polymeric systems by conducting microscopic simulations with known force fields, and fitting the extracted fluctuation amplitudes with theoretical expressions as we have done for our model system. In this respect, DNA is of particular interest: a recently developed open-boundary molecular dynamics of a DNA molecule in explicit salt–hybrid explicit/implicit water solution<sup>[39]</sup>

would enable DNA simulations at lower, physiological salt concentrations  $\sim 0.15$  M. At this stage, let us make an estimate of the coupling strength for DNA, making use of the theoretical prediction in Equation (9). Assuming a persistence length  $\xi_p \sim 50$  nm and chains much longer than that, a sub-nematic DNA concentration  $5 \text{ mg mL}^{-1}$  (with the atomic mass of 650 dalton/base pair and the length 0.33 nm/base pair this amounts to a total length per unit volume of  $\rho_0 l_0 \approx 1.5 \text{ mm } \mu\text{m}^{-3}$ ) and temperature 300 K, one gets  $\tilde{G} = G(\frac{2}{3}\rho_0 l_0)^2 \approx \frac{2}{3}k_B T \xi_p \rho_0 l_0 \approx 2 \times 10^{-13}$  N. This is expected to be at least comparable if not much larger than the elastic constant  $L$  (in the case of the simulated  $N_s = 128$  chains, we get  $\tilde{G}/L \sim 20$ ). Consequently, the expected induced nematic ordering is of the same order of magnitude as the relative variation of the polymer concentration.

## 5. Conclusions

We have established a tensorial description of coupled density–nematic order fluctuations in the isotropic phase of linear polymer melts/solutions. We have validated and confirmed the proposed tensorial conservation law, which connects density and orientational order, by running extensive Monte Carlo simulations of isotropic polymer melts composed of worm-like chains with variable length and flexibility. This coupling induces orientational order as a consequence of density/concentration variations, which can be macroscopically relevant even in an otherwise isotropic polymeric liquid. Our results show that these effects become increasingly important in particular as the chains get stiffer. Rather surprisingly, the coupling is notable also for extremely short chains (a few monomers). Moreover, we have alluded to the possible relevance of symmetry-allowed coupling between chain curvature and other system variables, and presented means of its quantification. Our multiscale formalism is general and robust and provides a way to construct bottom-up continuum models of polymer melts/solutions, for example, dense ordered DNA phases, by allowing us to extract the unknown parameters of the continuum models from microscopic simulations or scattering experiments.<sup>[40–42]</sup>

The average chain curvature as a macroscopic variable is not normally encountered. Governing the strength of the density–nematic coupling, it is, however, relevant for the static macroscopic response of line polymers and therewith accessible from the macroscopic level. In this perspective, experimental detection and characterization of the ensuing acoustic/osmotic birefringence represents an exciting scientific challenge to be pursued in the future.

## 6. Methodology

Methods, including numerical simulation details, derivation of the tensorial conservation law, free-energy functional and correlation functions, theoretical models of the sources, and of the coupling strength can be found in the Supporting Information.

## Supporting Information

Supporting Information is available from the Wiley Online Library or from the author.

## Acknowledgements

The authors' special appreciation and gratitude goes to Kostas Ch. Daoulas for contributing the soft WLC model, sharing the simulation code, offering his experience, and participating in numerous valuable discussions throughout this long-lasting investigation. The authors acknowledge financial support through grants P1-0002 and J1-7435 from the Slovenian Research Agency.

## Conflict of Interest

The authors declare no conflict of interest.

## Keywords

induced birefringence, linear polymers, Monte Carlo, polymer melt/solution, tensorial conservation law

Received: January 29, 2019

Revised: March 8, 2019

Published online: April 4, 2019

- [1] L. G. Fel, *Phys. Rev. E* **1995**, 52, 702.
- [2] D. R. Nelson, *Phys. A* **1991**, 177, 220.
- [3] R. D. Kamien, D. R. Nelson, *J. Stat. Phys.* **1993**, 71, 23.
- [4] D. R. Nelson, *Defects and Geometry in Condensed Matter Physics*, Cambridge University Press, Cambridge **2002**.
- [5] D. Svenšek, G. M. Grason, R. Podgornik, *Phys. Rev. E* **2013**, 88, 052603.
- [6] P. G. de Gennes, *Mol. Cryst. Liq. Cryst.* **1976**, 34, 177.
- [7] R. B. Meyer, *Polymer Liquid Crystals*, (Eds: A. Ciferri, W. R. Krigbaum, R. B. Meyer), Academic Press **1982**, p. 133.
- [8] G. J. Vroege, T. Odijk, *Macromolecules* **1988**, 21, 2848.
- [9] X. Ao, X. Wen, R. B. Meyer, *Phys. A* **1991**, 176, 63.
- [10] J. V. Selinger, R. F. Bruinsma, *Phys. Rev. A* **1991**, 43, 2910.
- [11] P. Le Doussal, D. R. Nelson, *Europhys. Lett.* **1991**, 15, 161.
- [12] R. D. Kamien, P. Le Doussal, D. R. Nelson, *Phys. Rev. A* **1992**, 45, 8727.
- [13] J. V. Selinger, R. F. Bruinsma, *J. Phys. II* **1992**, 2, 1215.
- [14] A. Popadič, D. Svenšek, R. Podgornik, K. C. Daoulas, M. Praprotnik, *Soft Matter* **2018**, 14, 5898.
- [15] D. Svenšek, R. Podgornik, *Phys. Rev. E* **2016**, 93, 052703.
- [16] M. S. Shell, *J. Chem. Phys.* **2008**, 129, 144108.
- [17] W. G. Noid, *J. Chem. Phys.* **2013**, 139, 090901.
- [18] T. T. Foley, M. S. Shell, W. G. Noid, *J. Chem. Phys.* **2015**, 143, 243104.
- [19] J. Zavadlav, R. Podgornik, M. Praprotnik, *Sci. Rep.* **2017**, 7, 4775.
- [20] R. Podgornik, J. Zavadlav, M. Praprotnik, *Computation* **2018**, 6, 3.
- [21] D. Svenšek, G. Veble, R. Podgornik, *Phys. Rev. E* **2010**, 82, 011708.
- [22] D. Svenšek, R. Podgornik, *Europhys. Lett.* **2012**, 100, 66005.
- [23] W. Reisner, K. J. Morton, R. Riehn, Y. M. Wang, Z. Yu, M. Rosen, J. C. Sturm, S. Y. Chou, E. Frey, R. H. Austin, *Phys. Rev. Lett.* **2005**, 94, 196101.
- [24] D. Gupta, J. J. Miller, A. Muralidhar, S. Mahshid, W. Reisner, K. D. Dorfman, *ACS Macro Lett.* **2015**, 4, 759.
- [25] L. Delle Site, M. Praprotnik, *Phys. Rep.* **2017**, 693, 1.
- [26] M. Praprotnik, L. Delle Site, K. Kremer, *Annu. Rev. Phys. Chem.* **2008**, 59, 545.
- [27] A. Ramírez-Hernández, S.-M. Hur, J. C. Armasérez, M. O. d. I. Cruz, J. J. De Pablo, *Polymers* **2017**, 9, 88.
- [28] A. Milchev, S. A. Egorov, K. Binder, A. Nikoubashman, *J. Chem. Phys.* **2018**, 149, 174909.

- [29] K. Kremer, G. S. Grest, *J. Chem. Phys.* **1990**, *92*, 5057.
- [30] P. Gemünden, K. C. Daoulas, *Soft Matter* **2015**, *11*, 532.
- [31] D. Frenkel, B. Smit, *Understanding Molecular Simulation: From Algorithms to Applications*, 2nd ed., Academic Press, San Diego **2001**.
- [32] M. Tuckerman, *Statistical Mechanics: Theory and Molecular Simulation*, Oxford University Press, Oxford **2010**.
- [33] G. S. Grest, K. Kremer, T. A. Witten, *Macromolecules* **1987**, *20*, 1376.
- [34] G. S. Grest, K. Kremer, S. T. Milner, T. A. Witten, *Macromolecules* **1989**, *22*, 1904.
- [35] J. Sablić, M. Praprotnik, R. Delgado-Buscalioni, *Soft Matter* **2016**, *12*, 2416.
- [36] J. Sablić, M. Praprotnik, R. Delgado-Buscalioni, *Soft Matter* **2017**, *13*, 4971.
- [37] J. Sablić, R. Delgado-Buscalioni, M. Praprotnik, *Soft Matter* **2017**, *13*, 6988.
- [38] J. V. Selinger, M. S. Spector, V. A. Greanya, B. T. Weslowski, D. K. Shenoy, R. Shashidhar, *Phys. Rev. E* **2002**, *66*, 051708.
- [39] J. Zavadlav, J. Sablić, R. Podgornik, M. Praprotnik, *Biophys. J.* **2018**, *114*, 2352.
- [40] X. AO, R. B. Meyer, *Physica A* **1991**, *176*, 63.
- [41] V. G. Taratuta, A. J. Hurd, R. B. Meyer, *Phys. Rev. Lett.* **1985**, *55*, 246.
- [42] L. C. A. Groot, M. E. Kuil, J. C. Leyte, J. R. C. van der Maarel, *Liq. Cryst.* **1994**, *17*, 263.